Journal of Magnetic Resonance **145,** 125–131 (2000)
doi:10.1006/jmre.2000.2083, available online at http://www.idealibrary.com on IDEAL®

Thermal Convection Currents in NMR: Flow Profiles and Implications for Coherence Pathway Selection

Alexej Jerschow[1]

Materials Sciences Division, Lawrence Berkeley Laboratory, and Chemistry Department, Hildebrand D62, University of California at Berkeley, Berkeley, California 94720; and Section de Chimie, Université de Lausanne, CH-1015 Lausanne, Switzerland

E-mail: ajerschow@lbl.gov

Received January 12, 2000; revised March 15, 2000

Rayleigh–Bénard convection currents are visualized in a vertical cylindrical tube by means of magnetic resonance imaging. Axially antisymmetric flow, multiple vertical rolls, and twisted node planes are observed. The flow can also be induced by strong RF irradiation. Its effects on the coherence pathways in NMR experiments employing field gradients are discussed. © 2000 Academic Press

Key Words: **Rayleigh–Bénard convection; free convection; flow; magnetic resonance imaging; coherence pathway selection.**

1. INTRODUCTION

A fluid layer exposed to a temperature gradient over its height is known to produce flow driven by buoyancy forces. Convection occurs when the heat transported by thermal conduction is not sufficient to maintain mechanical equilibrium. Characteristic roll patterns are predicted from theory and seen experimentally (*1*).

A particularly interesting case—from the point of view of applications—is free convection in a vertical cylinder, which has been investigated in great detail both theoretically and experimentally (*2–5*).

Magnetic resonance imaging (MRI) can be easily applied to obtain three-dimensional images and images along arbitrary planes, unlike many optical techniques (*6*). Furthermore, the susceptibility to disturbances caused by dust particles is practically nonexistent. MRI is used extensively for flow studies (see for example Refs. *25, 26*). Recently, MRI was used to visualize thermal convection in porous media (*7*) and in a flat horizontal layer (*8*).

In this publication free convective flow is visualized and analyzed in a vertical cylinder of moderate aspect ratio ($\eta = 9$ and 3.3) by MRI. The results agree well with the theory of Ostroumov (*2*) for infinite cylinders. Variable temperature experiments were conducted with different solvents. Multiple roll patterns and a twist in the nodal plane were also observed, as predicted by theory (*9–11*). The velocities measured agree well with the ones obtained by Loening and Keeler (*12*), who used a nonlocalized multiple PGSE NMR experiment in a similar setup.

Convective flow has been shown to produce a number of artifacts in standard nuclear magnetic resonance (NMR) experiments (*13–15*), sometimes leading to complete signal disappearance. In these cases it is necessary to take into account the particular properties of the flow. It is also shown that similar flow patterns can be produced by intense RF irradiation, as is the case in heteronuclear decoupling. The artifacts produced by the convection currents are of an attenuating nature and depend on the coherence pathways. The effects could therefore be used for coherence pathway selection. The underlying principles will be discussed.

2. THEORY

We consider here the free convection induced by a linear temperature gradient in a vertical cylinder of radius R and height h. In what follows, the theory of Ostroumov (*2*) will be reviewed. The points of departure are the following equations:

$$\dot{\mathbf{v}} + (\mathbf{v}\nabla)\mathbf{v} = -\frac{\nabla p}{\rho} + \mathbf{g}\beta T + \nu\Delta\mathbf{v}, \qquad [1]$$

$$\dot{T} + \mathbf{v}\cdot\nabla T = \chi\Delta T, \qquad [2]$$

$$\dot{\rho} + \nabla(\rho\mathbf{v}) = 0, \qquad [3]$$

which are the Navier–Stokes, the heat conduction/convection, and the continuity equations. Here, $\mathbf{v}$ is the velocity, p the pressure, ρ the density, $\mathbf{g}$ the gravitational acceleration, β the expansion coefficient, T the temperature measured from a convenient reference point, ν the kinematic viscosity, and χ the thermal diffusivity. Looking for the steady solution, using the Boussinesq approximation (*1*) $\nabla\rho = 0$ and assuming the fluid to move along parallel streamlines along z (the vertical direction) gives $\partial v/\partial z = 0$ with $v = v_z$. Assuming further that

[1] Correspondence should be addressed at the University of California at Berkeley.

1090-7807/00 $35.00
Copyright © 2000 by Academic Press
All rights of reproduction in any form reserved.

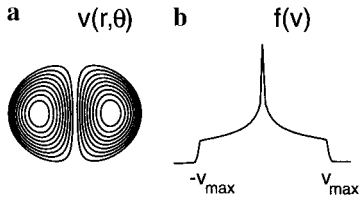

FIG. 1. Theoretical velocity profile corresponding to the lowest antisymmetric mode $n = 1$ for Ra = 100 according to Eq. [9]. For water at 325 K in a cylinder of radius 2.1 mm this corresponds to a temperature gradient of about 1 K/cm. (a) Circular cross section. The node line divides the regions of positive and negative velocity. (b) Velocity distribution.

$\partial T/\partial x = \partial T/\partial y = 0$ and $\nabla p = 0$ (no external pressure gradient), the following equations are obtained:

$$-g\beta T + \nu\Delta v = 0, \quad [4]$$

$$\Gamma v - \chi\Delta T = 0. \quad [5]$$

where $\Gamma = \partial T/\partial z$.

Applying Δ to Eq. [4] and inserting [5] gives

$$(\Delta\Delta - k^4)v = 0 \quad [6]$$

with $k^4 = g\beta\Gamma/\nu\chi$. The general solution of [6] satisfying the boundary conditions

$$v\ (r = R) = 0 \quad \text{(at wall)} \quad [7]$$

$$v\ (r = 0) = \text{finite} \quad [8]$$

is

$$v = \sum_{n=0}^{\infty} v_n \left(\frac{I_n(kr)}{I_n(kR)} - \frac{J_n(kr)}{J_n(kR)} \right) \cos n\phi, \quad [9]$$

where J_n and I_n are the Bessel and modified Bessel functions of the first kind. Using thermal boundary conditions the lowest critical Rayleigh numbers $\text{Ra} = (kR)^4 = g\beta\Gamma R^4/(\nu\chi)$ are found for $n = 1$. They are 67.4 for insulating and 215.8 for perfectly conducting surrounding media (strictly speaking this is only true for a cylinder drilled in some material, but the structure of the equations is the same for a cylinder with a wall of a different material than the surrounding medium; some corrections apply in this case (*2*)).

Figure 1 shows the velocity distribution predicted from Eq. [9] for the lowest azimuthal mode ($n = 1$).

It is evident that the above treatment will not be realistic for a bounded cylinder, where flow in the x or y directions must occur. For such a case multiple vertical rolls are predicted. The critical Ra numbers for m vertical rolls are (*9*)

$$\text{Ra}_{cr} = \frac{1}{(k_n R)^2} \left[(k_n R)^2 + \left(\frac{m\pi}{\eta} \right) \right]^3, \quad [10]$$

where k_n corresponds to an eigenmode with azimuthal mode number n, and $\eta = h/(2R)$ is the aspect ratio. Azimuthal modes with n other than 1 are unlikely to occur for the aspect ratios considered here ($\eta > 1$) (*16, 17*), so the velocity profile is expected to be of the form shown in Fig. 1. As the aspect ratio becomes larger the critical Ra numbers for the different vertical modes move closer together and multiple rolls appear (*9*). A twist in the nodal plane is predicted (*10, 11*), occurring probably as a transient between modes. This was indeed found in the experiment.

3. EXPERIMENTAL

For the visualization of the convective flows a velocity encoded MRI pulse sequence was used (Fig. 2) (*18, 19*). Before pulse four in the sequence the moving spins will have acquired a phase factor

$$\exp(-i\phi) = \exp(-i\gamma G_v v \delta\Delta), \quad [11]$$

where γ is the gyromagnetic ratio, G_v the strength of the

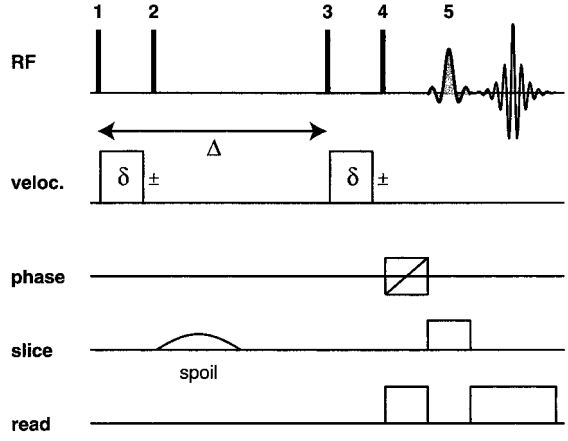

FIG. 2. Velocity encoded MRI pulse sequence. Pulses 1–4 are hard 90° pulses (duration 10 μs); pulse 5 is a sinc-shaped soft pulse over 2.5 periods with 2-ms duration exciting a slice of approximately 1.4-mm thickness. The velocity encoding gradients were of 0.195 T/m strength and 1-ms duration. $\Delta = 50$ ms. The phase encoding gradient was ramped in 32 increments from -0.05 to 0.05 T/m and switched on for 1 ms. The spoiler gradient was sine shaped with a peak strength of 0.15 T/m and 3-ms duration. The read gradient was turned on for 1 ms before pulse 5 and during the acquisition with a strength of 0.1 T/m. A total of 256 points were acquired in the direct dimension in intervals of 13 μs. A delay of 200 μs was included whenever a RF pulse directly followed a gradient. The phase cycle was: $\phi_1 = x, x, -x, -x$; $\phi_2 = \phi_5 = y$; $\phi_3 = y, y, y, y, -y, -y, -y, -y$; $\phi_4 = -x$, ϕ(receiver) $= x, -x, -x, x, -x, x, x, -x$, and the polarity of the velocity encoding gradients was flipped in consecutive scans as explained in the text and indicated by the $\pm$ sign. For the calibration experiment pulse 4 was removed and the receiver phase was ϕ(receiver) $= x, x, -x, -x, -x, -x, x, x$.

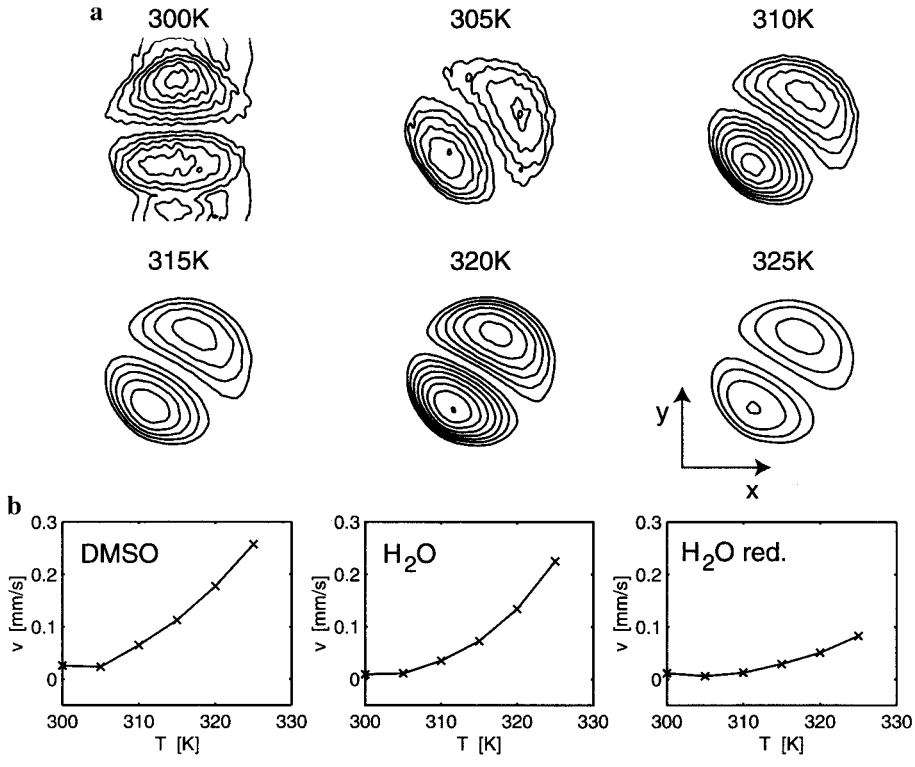

FIG. 3. (a) Velocity encoded images of slices through the circular cross-section of the cylinder (inner diameter 4.2 mm) at different temperatures for a sample of pure dimethyl sulfoxide (DMSO). The slice selection and velocity encoding gradients were performed along z and the phase encoding gradient along y. The read gradient was along x. (b) Temperature dependence of the maximum velocity observed using a calibration experiment for DMSO, water, and water with a reduced fill height, $h = 14$ mm ($\eta = 3.3$).

velocity encoding field gradient in T/m, δ the duration of the gradient pulse, and Δ the time from the start of the first gradient to the start of the second. Pulse five will rotate the cos ϕ component of the magnetization into z thus giving zero intensity for static spins. The velocity dependence of the signal intensity is given by the sin ϕ component. An appropriate phase cycle and a spoiler gradient were designed using the CCCP program (*20*) to remove artifacts. In addition to that the velocity encoding gradients were switched in sign in consecutive experiments along with the receiver phase for a cleaner selection of the sin ϕ component of the magnetization (*18, 19*). The velocity is calibrated by an experiment where the receiver phase does not follow the gradient cycle, thus obtaining the cos ϕ component of the magnetization (in addition pulse four has to be removed). After zero filling the raw data and Fourier transform, the images were represented in absolute value in order to rule out phase errors. This in no way decreased the ability to distinguish areas of positive and negative flow, since there were always clear node lines present. The number of scans was 8, the number of increments 32, and the number of points in the direct dimension was 256. The experiment took 10 min (a repetition delay of 2 s was used).

A standard 5 mm NMR tube was used for the experiments, with the active RF coil region positioned in the region of 10–26 mm from the bottom of the tube. The experiments were performed on a Bruker DRX600 (600 MHz) (Figs. 3, 4, and 6) and DRX300 (300 MHz) NMR spectrometers (Fig. 5), using multinuclear inverse TBI and TXI probes, respectively, and an Eurotherm VT2000 temperature regulation. An airflow of 100 L/h was used throughout. The height of the liquid was 3.7 cm unless stated otherwise. The setup used in this work is known to produce a near-linear temperature gradient and precise temperature data are available for the range of experimental parameters used.

4. FLOW PROFILES

Figure 3 shows the results of the experiments performed at different temperatures for samples of dimethyl sulfoxide (DMSO), water, and water with a reduced fill height (to fit the active region of the RF coil). The maximum velocities are calculated using a calibration experiment as described above. The reduction in the sample volume has the effect of decreasing the maximum velocity by about a factor of 3. This is in qualitative agreement with the increase of the critical Ra number as given by Eq. [10]. DMSO shows a slightly higher velocity than water. Loening and Keeler (*12*) have used a thulium(III) complex for the accurate localized measurement of the temperature using the same setup. They determined the temperature gradient as approximately 1 K/cm for the highest

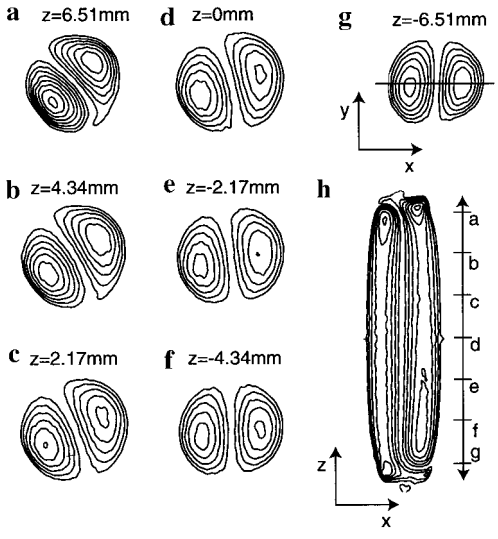

FIG. 4. (a–g) Observation of a twisted nodal plane with a sample of DMSO at 311 K. The slices are acquired at different positions along the cylinder. (h) Experiment with the velocity and phase encoding gradients along z (maximum strength 0.195 and 0.039 T/m, respectively). The z positions of the slices a–g are indicated. The slice selection is along y (0.075 T/m), and the read gradient along x (the solid line in (g) indicates the position of the slice.)

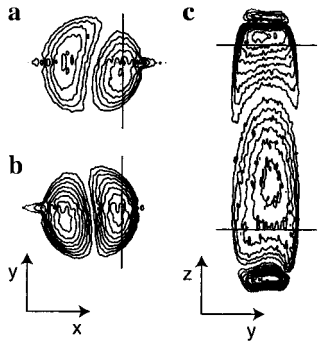

FIG. 5. Experiments on DMSO on a Bruker DRX300 (300 MHz) NMR spectrometer. Multiple rolls are observed here. (a, b) Circular cross sections at the top and at the bottom of the active volume; (c) image obtained with z phase and velocity encoding, x slice selection. Other parameters were the same as for Fig. 4h. The solid lines indicate the positions of the slices.

temperature setting (325 K) and accordingly smaller gradients for lower temperatures. The velocities measured in a nonlocalized PGSENMR experiment agree well with the ones reported here.

Figure 4 shows experiments on DMSO at 311 K. The slices were taken at different z positions along the cylinder. The node plane is seen to rotate as predicted by Normand (*10, 11*). The pitch of the helix is about 3.5°/mm. The maximum velocities are fairly constant over the slices (within experimental uncertainty): 0.63, 0.63, 0.56, 0.54, 0.50, 0.51, and 0.58 mm/s (from top to bottom). Figure 4h shows the image along the $x - z$ plane with z velocity encoding and y slice selection. The increase in intensity from the bottom to the top on the right-hand side is due to the twist of the nodal plane (the same is true for the left-hand side in the inverse direction). The apparent additional nodes at the very top and bottom are probably caused by the nonideal behavior of the pulse sequence at the edges of the active region (B_1 inhomogeneity and gradient nonlinearity (*21*)).

Figure 5 shows the occurrence of multiple rolls in a sample of DMSO on a different instrument (300-MHz spectrometer), where the geometry of the probe is slightly different. The node plane of the upper roll is also rotated slightly with respect to the lower one. It is possible that in this case nonlinear temperature gradients (*22*) play a role, all other conditions being the same as in the previous experiments. Efforts are underway to investigate the temperature distribution more closely by means of a suitably accurate NMR temperature shift reagent.

No significant time variations of the velocities or the positions of the nodal planes were observed in any of the experiments, probably due to signal averaging over the course of the experiment.

In another experiment the buoyancy forces were generated by heat from prolonged RF irradiation, as is common in NMR (Fig. 6). The flow pattern always formed with the nodal plane along the same direction, indicating that the geometry of the RF coil plays a major role. The same flow pattern formed, and the maximum velocity was 0.18 mm/s, thus being comparable to the flow velocities produced by the "natural" temperature gradients in Fig. 3.

5. IMPLICATIONS FOR COHERENCE PATHWAY SELECTION

Convective flow has been shown to produce severe artifacts in NMR experiments employing pulsed field gradients (*13–15*). In this section we state how the flow affects different coherence pathways and how it can in principle be used for coherence pathway selection. This was already alluded to in two previous publications (*14, 20*) but was stated without referring to the actual flow pattern.

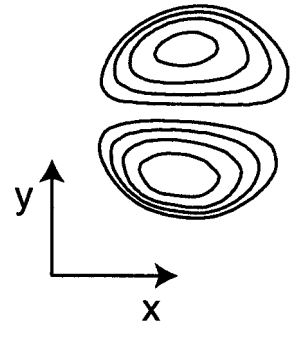

FIG. 6. A slice along the circular cross section for an experiment with DMSO where 31-kHz multiple pulse GARP decoupling (*24*) was turned on for 200 ms before every scan on the carbon-13 channel, thus heating the sample and causing convection currents.

Thermal convection in combination with pulsed field gradients leads to the appearance of phase factors depending on the gradient strength, the velocity, and the traversed coherence pathways. The dispersion of the convection velocities over the sample leads to an effective attenuation of the signals arising from different pathways.

A signal following a particular pathway acquires the phase

$$\phi(\mathbf{r}) = \int_0^t \gamma \mathbf{G}^*(t') \cdot \mathbf{r}(t') dt', \qquad [12]$$

where $\mathbf{G}^*(t) = p(t)\mathbf{G}(t)$ is the effective gradient (*18, 20*), p the coherence order, and $\mathbf{r}$ the location of the spin in the sample. Heteronuclear cases are encompassed in this description by using the composite coherence order (*23*) $p_c = \sum_i \gamma_i p_i / \gamma_1$, where the sum runs over all occurring nuclei.

Using the expansion $\mathbf{r} = \mathbf{r}_0 + \mathbf{v}t + \frac{1}{2}\mathbf{a}t^2 + \ldots$ we can write

$$\phi(\mathbf{r}) = \mathbf{r}_0 \underbrace{\int_0^t \gamma \mathbf{G}^*(t') dt'}_{\text{zeroth moment}} + \mathbf{v} \underbrace{\int_0^t \gamma \mathbf{G}^*(t') t' dt'}_{\text{first moment}} + \tfrac{1}{2}\mathbf{a} \underbrace{\int_0^t \gamma \mathbf{G}^*(t') t'^2 dt'}_{\text{second moment}} + \ldots \qquad [13]$$

The zeroth moment corresponds to matching the gradient echo condition (for static spins). All higher moments introduce additional constant phase shifts if $\mathbf{v}$, $\mathbf{a}$, and the higher derivatives are kept the same for the duration of the experiment. For simplicity we shall be concerned only with $\mathbf{v}$ being constant and nonzero (i.e., no flow acceleration). In this case only a phase factor proportional to the velocity is introduced. With a velocity distribution $f(\mathbf{v})$ present in the sample, the ensemble average results in a signal attenuation

$$F = \int f(\mathbf{v}) \exp(-i\phi(\mathbf{v})) d\mathbf{v}, \qquad [14]$$

where the integral is taken over the ranges of the velocities v_x, v_y, v_z, and $\phi(\mathbf{v}) = \mathbf{v} \int_0^t \gamma \mathbf{G}^*(t') t' dt'$.

Figure 7a illustrates how the phase is calculated for a given coherence pathway. The zeroth moment for this pathway is zero (i.e., the echo condition is fulfilled), but the phase due to flow is nonzero resulting in signal attenuation. Figure 7b shows another pathway, for which both the zeroth and the first moments are zero, resulting in no signal attenuation. This would be an example of a coherence pathway selection setup using free convective flow. The two pathways are both refocused by the gradients in the static case. Convective flow, however, leads to the attenuation of one of them. In practice one can adjust the timings and the gradient strengths in order to achieve a simultaneous nulling of the zeroth and the first moments. A similar trick has been applied for the convection compensated GOESY and GROESY experiments (*14*).

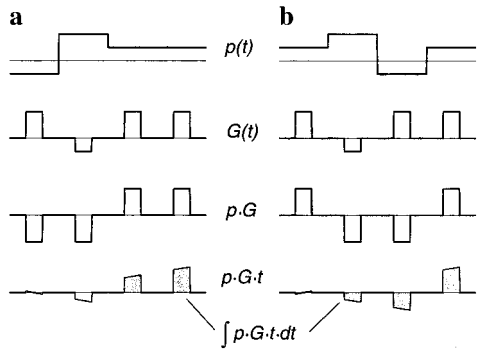

FIG. 7. Calculation of $\phi(\mathbf{v}_0)$ for two different coherence pathways which satisfy the echo condition (i.e., the integral over the effective gradient is zero, $\int G(t)p(t)dt = 0$) and a given sequence of field gradients. (a) A pathway acquiring a nonzero phase due to motion. (b) A pathway, refocusing both the zeroth and the first moments of the gradient leading to no signal loss due to convective flow. The phase factor is proportional to the shaded area under the curves at the bottom. The overall signal attenuation is found from this factor by integrating over the velocity profile according to Eq. [16]. The time origin is set at the center of the first gradient pulse.

The actual signal attenuation is now calculated for a given phase $\phi(\mathbf{v}_0)$ and a flow profile of the first (and most common) mode in the convection flow pattern (i.e., $n = 1$) using Eqs. [9], [11], and [14]:

$$F = \frac{1}{\pi R^2} \int_0^R \int_0^{2\pi} \times \exp\left[i\phi(v_0) \left(\frac{I_1(kr)}{I_1(kR)} - \frac{J_1(kr)}{J_1(kR)} \right) \cos\theta \right] r dr d\theta. \qquad [15]$$

This can be reduced to a one-dimensional integral, and using the dimensionless quantities $\kappa_0 = kR$ and $\kappa = kr$ one gets

$$F = \frac{2}{\kappa_0^2} \int_0^{\kappa_0} J_0\left[\phi(v_0) \left(\frac{I_1(\kappa)}{I_1(\kappa_0)} - \frac{J_1(\kappa)}{J_1(\kappa_0)} \right) \right] \kappa d\kappa. \qquad [16]$$

Apparently this form may not be reduced any further and the calculation of the attenuation factors has to be performed numerically. Figure 8 shows the signal attenuation functions for different flow regimes. It is interesting to note that unlike the attenuation factors due to the gradients in the static case the signal here does not drop below zero, except for very low

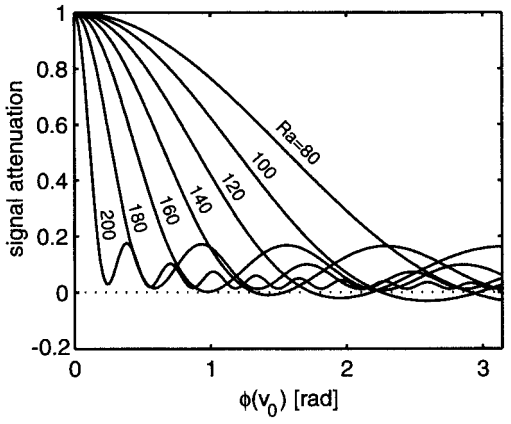

FIG. 8. Calculation of the overall signal attenuation as a function of $\phi(\nu_0)$ according to Eq. [16]. The Rayleigh numbers 80, 100, 120, 140, 160, 180, and 200 correspond to temperature gradients of about 0.8, 1.0, 1.2, 1.4, 1.6, 1.8, and 2 K/cm for water at 325 K.

Rayleigh numbers. A behavior of this type is also witnessed experimentally in Fig. 1 of Ref. (*14*). A gradient strength of just 0.094 T/m in a gradient echo with a gradient duration of 2 ms, a spacing of 100 ms, and a maximum flow velocity of 0.2 mm/s will produce a phase of 1 rad. At this point most flow profiles will produce a substantial signal attenuation. For Ra = 200, the signal will be attenuated to 7% of its original size. For higher order coherences the gradient strength necessary to achieve a certain attenuation factor is accordingly lower, similar to the case of coherence pathway selection via pulsed field gradients in the static case.

To summarize, coherence pathway selection via the convection currents can be achieved by choosing the gradient timings and strengths, such that the first moment of the effective gradient for the desired pathways is zero (in addition to the zeroth moment), and a large value for the unwanted pathways. Under conventional NMR conditions the free convection currents are reasonably well controllable and allow for a reproducible coherence pathway selection process.

6. CONCLUSIONS

Free convection flow patterns in a vertical cylinder were visualized by means of MRI. They agree well with Ostroumov's theory (*2*) for infinite vertical cylinders. The appearance of multiple rolls and a twist of the nodal plane were confirmed experimentally (*10, 11*). Combined with a proper NMR thermometer (*12, 22*) MRI is an ideal method for verifying theoretical predictions of flow behavior. The knowledge of the actual flow pattern is very important for NMR employing pulsed field gradients. Serious artifacts can arise and must be taken care of in NMR experiments (*13–15*). These are better understood with a detailed view on the flow pattern. While generic temperature gradients may be avoidable, strong RF irradiation and the use of strong pulsed field gradients are not and will also cause convective flow. Deliberate RF irradiation, on the other hand, can be used for the creation of "customized" temperature gradients. The convection currents can be put to good use in NMR for coherence pathway selection of which the principles have been laid out in this article.

ACKNOWLEDGMENTS

This work was supported by an Erwin Schrödinger fellowship of the Austrian Science Fund, by the Fonds National de la Recherche Scientifique (Switzerland), Grant 2160-53313-98, by the Commission pour la Technologie et l'Innovation (Switzerland), and by the Director, Office of Basic Energy Sciences, Materials Sciences Division, U.S. Department of Energy, under Contract DE-AC03-76SF00098.

REFERENCES

1. P. K. Kundu, "Fluid Mechanics," Academic Press, New York, 1990.
2. G. A. Ostroumov, Svobodnaja konvekzija v uslovijach vnutrennej zadachi, *Gosud. Izd. Techn.-Teor. Lit. Moscow* (1952).
3. G. Z. Gershuni and E. M. Zhukovitskii, "Convective Stability of Incompressible Fluids," Keter, Jerusalem, 1976.
4. M. A. Azouni, Evolution of non linear flow structure with aspect ratio, *Comm. Heat Mass Transfer* **14,** 447–456 (1987).
5. M. A. Azouni, Oscillatory behavior in cenvecting water, *Int. J. Heat Mass Transfer* **24,** 1983–1986 (1981).
6. W. Merzkirch, "Flow Visualization," Academic Press, New York, 1987.
7. M. D. Shattuck, R. P. Behringer, G. A. Johnson, and J. G. Georgiadis, Convection and flow in porous media. Part 1. Visualization by magnetic resonance imaging, *J. Fluid Mech.* **332,** 215–245 (1997).
8. S. J. Gibbs, T. A. Carpenter, and L. D. Hall, Magnetic resonance imaging of thermal convection, *J. Magn. Reson. A* **105,** 209–214 (1993).
9. C. Guthmann, B. Perrin, and H. Thomé, Non-linear behavior of convection in a vertical cylindrical cell at high aspect ratio, *J. Phys. France* **50,** 2951–2965 (1989).
10. C. Normand, Nonlinear convection in high vertical channels, *J. Fluid Mech.* **143,** 223–242 (1984).
11. C. Normand, Phase instabilities for antisymmetric convective flows in a vertical cylinder, *Phys. D* **39,** 267–280 (1989).
12. N. M. Loening and J. Keeler, Measurement of convection and temperature profiles in liquid samples, *J. Magn. Reson.* **139,** 334–341 (1999).
13. A. Jerschow and N. Müller, Suppression of convection artifacts in stimulated echo diffusion experiments: double stimulated echo experiments, *J. Magn. Reson.* **125,** 372–375 (1997).
14. A. Jerschow and N. Müller, Convection compensation in gradient enhanced nuclear magnetic resonance spectroscopy, *J. Magn. Reson.* **132,** 13–18 (1998).
15. J. Lounila, K. Oikarinen, P. Ingman, and J. Jokisaari, Effects of thermal convection on NMR and their elimination by sample rotation, *J. Magn. Reson. A* **118,** 50–54 (1996).
16. G. S. Charlson and R. L. Sani, Thermoconvective instability in a

bounded cylindrical fluid layer, *Int. J. Heat Mass Transfer* **13,** 1479–1496 (1970).

17. G. S. Charlson and R. L. Sani, On thermoconvective instability in a bounded cylindrical fluid layer, *Int. J. Heat Mass Transfer* **14,** 2157–2160 (1971).
18. P. T. Callaghan, "Principles of Nuclear Magnetic Resonance Microscopy," Clarendon Press, Oxford, 1993.
19. D. Bourgeois and M. Decorps, Quantitative imaging of slow coherent motion by stimulated echoes with suppression of stationary water signal, *J. Magn. Reson.* **94,** 20–33 (1991).
20. A. Jerschow and N. Müller, Efficient simulation of coherence transfer pathway selection by phase cycling and pulsed field gradients in NMR, *J. Magn. Reson.* **134,** 17–29 (1998).
21. A. Jerschow and G. Bodenhausen, Mapping the B_1 field distribution with non-ideal gradients in a high-resolution NMR spectrometer, *J. Magn. Reson.* **137,** 108–115 (1999).
22. N. Hedin and I. Furó, Temperature imaging by ^{1}H NMR and suppression of convection in NMR probes, *J. Magn. Reson.* **131,** 126–130 (1998).
23. L. Mitschang, H. Ponstingl, D. Grindrod, and H. Oschkinat, Geometrical representation of coherence transfer selection by pulsed field gradients in high-resolution nuclear magnetic resonance, *J. Chem. Phys.* **102,** 3089–3098 (1995).
24. A. J. Shaka, P. B. Barker, and R. Freeman, Computer-optimized decoupling scheme for wideband applications and low-level operations, *J. Magn. Reson.* **64,** 547–552 (1985).
25. J. D. Seymour, B. Manz, and P. T. Callaghan, Pulsed gradient spin echo nuclear magnetic resonance measurements of hydrodynamic instabilities with coherent structure: Taylor vortices, *Phys. Fluids* **11,** 1104–1113 (1999).
26. B. Manz, J. D. Seymour, and P. T. Callaghan, PGSE NMR observations of convection in a capillary, *J. Magn. Reson.* **125,** 153–158 (1997).